

pubs.acs.org/JPCA Article

Unraveling the Vibrational Spectral Signatures of a Dislocated H Atom in Model Proton-Coupled Electron Transfer Dyad Systems

Liangyi Chen, Edwin L. Sibert III,* and Joseph A. Fournier*



Cite This: https://doi.org/10.1021/acs.jpca.3c00524



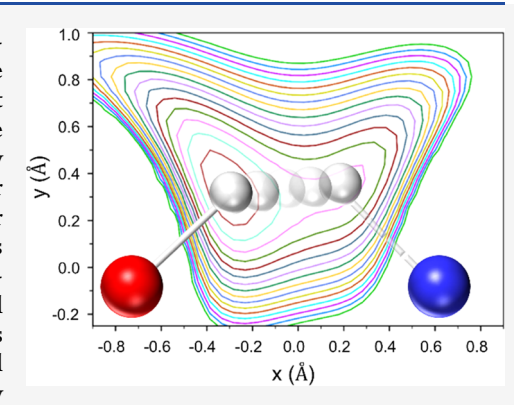
ACCESS I

III Metrics & More

Article Recommendations

SI Supporting Information

ABSTRACT: Phenol—benzimidazole and phenol—pyridine proton-coupled electron transfer (PCET) dyad systems are computationally investigated to resolve the origins of the asymmetrically broadened H-bonded OH stretch transitions that have been previously reported using cryogenic ion vibrational spectroscopy in the ground electronic state. Two-dimensional (2D) potentials describing the strongly shared H atom are predicted to be very shallow along the H atom transfer coordinate, enabling dislocation of the H atom between the donor and acceptor groups upon excitation of the OH vibrational modes. These soft H atom potentials result in strong coupling between the OH modes, which exhibit significant bend-stretch mixing, and a large number of normal mode coordinates. Vibrational spectra are calculated using a Hamiltonian that linearly and quadratically couples the H atom potentials to over two dozen of the most strongly coupled normal modes treated at the harmonic level. The calculated vibrational spectra qualitatively



reproduce the asymmetric shape and breadth of the experimentally observed bands in the 2300–3000 cm⁻¹ range. Interestingly, these transitions fall well above the predicted OH stretch fundamentals, which are computed to be surprisingly red-shifted (<2000 cm⁻¹). Time-dependent calculations predict rapid (<100 fs) relaxation of the excited OH modes and instant response from the lower-frequency normal modes, corroborating the strong coupling predicted by the model Hamiltonian. The results highlight a unique broadening mechanism and complicated anharmonic effects present within these biologically relevant PCET model systems.

INTRODUCTION

Proton-coupled electron transfer (PCET) processes are vitally important throughout biology and chemistry. 1,2 One of the best-known and studied examples involves the strongly Hbonded Tyrz-His₁₉₀ pair located near the oxygen-evolving complex (OEC) in Photosystem II.^{3,4} Tyr₇ mediates electron transfer from the OEC to photo-oxidized cytochrome P680. These electron transfer events are accompanied by concerted proton transfer from Tyr_Z to His₁₉₀. Due to the significance of the Tyr_Z-His₁₉₀ pair, there have been many studies exploring PCET kinetics within model Tyr-His systems. 5-11 In particular, Hammarström and co-workers have performed time-resolved electronic spectroscopy on a series of phenolbenzimidazole and phenol-pyridine dyad molecules where photoexcitation of an electron-accepting moiety, like Ru-(bpy)₃²⁺, initiated electron transfer from phenol to the excited electron acceptor. Recovery of the electron acceptor's ground electronic state served as a measure of the PCET kinetics, with H vs D kinetic isotope effects being used to infer the mechanisms of the PCET reactions. While there is a clear correlation between measured PCET kinetics and proton donor-acceptor distance, quantitative modeling proved difficult, especially for dyads with very short (<2.6 Å) proton donor–acceptor distances. ¹³ The lack of agreement was attributed to the use of a simple Morse oscillator to model the proton potential energy surface. Additionally, variations of the proton donor—acceptor distance due to thermal excitation of low-frequency soft modes ("vibrational enhancement") are known to be critically important to PCET reaction dynamics. ^{14–19} It is evident that renewed studies are needed that directly target and more accurately model the proton transfer coordinate to better understand the proton transfer potential surface and its dependence on low-frequency vibrational motions.

To this end, we have recently reported vibrational spectra of several phenol—benzimidazole and phenol—pyridine dyad ions isolated and cryogenically cooled in the gas phase. ^{20,21} Three of these systems are shown in Figure 1 and are the focus of the present study. The three dyads are labeled BP, PP, and BB (B = benzimidazole, P = pyridine; the first letter indicates the protonated group *para* to the phenol OH, while the second letter indicates the H-bond acceptor group in the *ortho* position). The vibrational spectra of each model revealed highly red-shifted and extremely broadened features that were

Received: January 23, 2023 Revised: March 8, 2023



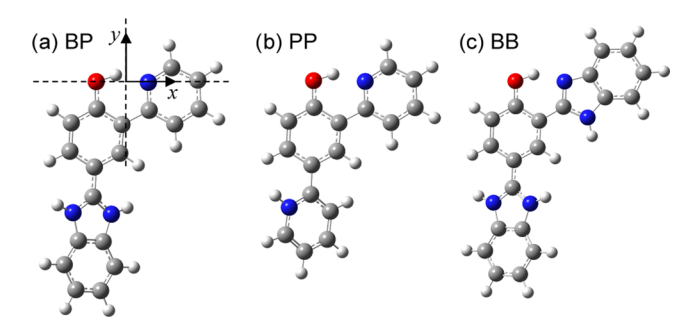


Figure 1. PCET model dyad systems. (a) BP, (b) PP, (c) BB. B = benzimidazole, P = pyridine. The first letter represents the protonated group *para* to the phenol OH. The second letter designates the H-bond acceptor group. The $\{x, y\}$ coordinate system for the H atom in-plane degrees of freedom is shown in panel (a).

assigned to the strongly H-bonded OH stretch transitions (Figure 2, red). These transitions each display relatively strong onsets near 2500 cm⁻¹ with weaker asymmetric shoulders that extend to >3000 cm⁻¹. Upon deuteration of the labile protons, weak and symmetrically broadened features appeared near 1900 cm⁻¹ that were assigned to the OD stretches (lower-frequency region of Figure 2). The red shifts in the frequency maxima in the OD and OH stretch regions follow the predicted proton donor—acceptor distances: PP < BP < BB.

Several computational strategies were employed to explain the extensive broadening observed in the OH and OD stretch regions. Harmonic calculations predicted significant OH bend character throughout many of the normal modes in the fingerprint region. This suggested that stretch-bend Fermi resonance interactions, a common broadening mechanism in strongly H-bonded systems, could be present. ^{22–24} Calculations revealed, however, that Fermi resonance interactions were expected to be minimal in the 2300–2600 cm⁻¹ range due to the red-shifted OH stretch transitions being largely out of resonance with overtones and combination bands involving the OH bend. ²⁰ It was concluded, therefore, that Fermi resonances play a minor role in the OH stretch broadening but

could contribute to some of the observed spectral substructures.

The other common broadening mechanism observed for strongly H-bonded OH/NH stretch transitions are Franck-Condon-like progressions that derive from the coupling of the high-frequency proton stretch to low-frequency soft modes along the donor-acceptor coordinate, 25-28 the same motions that drive vibrational enhancement of PCET kinetics in solution. We first calculated the dependence of the OH and OD stretch frequencies on variations in the lowest-frequency normal mode that significantly displaces the O-N proton donor-acceptor distance within the classical turning points at the zero-point level. The >300 and >200 cm⁻¹ variations predicted for the OH and OD stretch frequencies, respectively, with O-N displacement along the low-frequency normal mode could account for the experimentally observed breadth of the OH stretch onset features and the symmetrically broadened OD stretches. This simple model, however, did not account for the asymmetric OH stretch shoulders nor did it provide a more robust interpretation into the states involved that give rise to the broadening. To try to resolve these issues, we used a model Hamiltonian²⁸ that coupled the OH stretch to nearly a dozen additional low-frequency normal modes that showed large variations in the O-N donor-acceptor distance. Anharmonic calculations predicted sizeable (100-300 cm⁻¹) cubic coupling constants between the OH stretch and these soft modes. The model predicted a series of transitions, corresponding to numerous OH + soft-mode combination bands, that qualitatively accounted for the asymmetric shoulders in the OH stretch region. Although neither model was completely satisfactory, the results²¹ demonstrated the importance of the dependence and coupling of the OH stretches to a multitude of soft normal modes along the H atom transfer coordinate.

In a closely related study, Blodgett et al. reported the vibrational spectrum of methyl anthranilate in the S_1 excited electronic state. ²⁹ In this system, electronic excitation promotes the formation of a strong NH-O H-bond that is not present in the ground electronic state. Curiously, the expected H-bonded NH stretch transition was not observed in

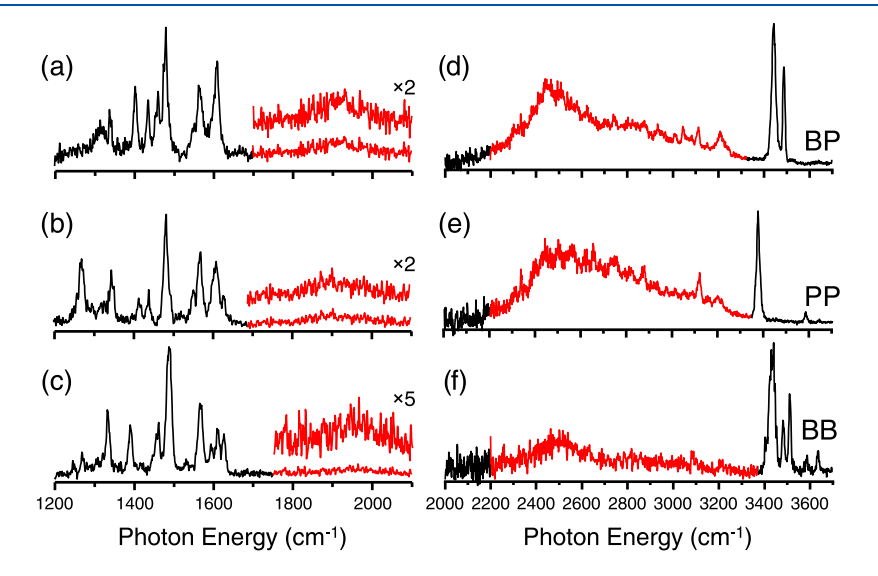


Figure 2. Cryogenic ion vibrational spectra of the dyad systems. (a, d) BP, (b, e) PP, (c, f) BB. Spectra for the deuterated isotopologues are shown in the lower-energy region in the left panels, with the presumptive OD stretch feature colored in red. Spectra for the light isotopologues in the higher-energy region are shown to the right, with the presumptive OH stretch feature colored in red.

the S₁ vibrational spectrum. Calculations that incorporated Fermi resonance interactions and Franck-Condon soft-mode coupling could not explain the absence of the NH stretch. An alternative approach was introduced in which a two-dimensional (2D) potential describing the stretching and in-plane bending degrees of freedom of the shared H atom was coupled to the remaining vibrational degrees of freedom.³⁰ The calculated H atom potentials were soft enough in the S₁ excited state to allow dislocation of the shared H atom upon NH stretch excitation. The H atom dislocation resulted in large changes in the forces along the other degrees of freedom, leading to strong coupling between the NH modes and numerous low-frequency modes. The S₁ vibrational spectrum predicted by coupling the excited-state H atom potential to 10 low-frequency modes revealed an extreme example of intensity sharing of the NH stretch bright state with a large number of background doorway states spanning >1000 cm⁻¹. An indirect coupling mechanism was identified where off-resonant NH + soft-mode doorway states are strongly coupled to doorway states in close resonance with the NH fundamental.

Herein, we apply the same approach used for methyl anthranilate to gain an improved understanding of the broadening mechanism at play in the PCET dyad systems. Quite surprisingly, the calculations reveal incredibly soft H atom potentials that result in significant dislocation of the H atom upon OH excitation in the ground electronic state. Consequently, the inclusion of more than two dozen strongly coupled normal modes is required in the model Hamiltonian. The predicted vibrational spectra qualitatively reproduce the lineshape profiles and spectral breadths in both the OH and OD stretch regions. Time-dependent calculations reveal ultrafast (<100 fs) relaxation of the excited OH modes into the lower-frequency normal modes. The results illustrate how significant high-order mechanical anharmonic effects that can couple a shared H atom or proton to the other vibrational degrees of freedom in very strongly H-bonded systems manifest in vibrational spectra.

■ EXPERIMENTAL METHODS

The cryogenic ion mass spectrometer has been described in detail previously. 20,31 Briefly, protonated ions were generated through electrospray ionization of \sim 200 μ M solutions of the dyad molecules in methanol with trace formic acid. Deuteration of the labile protons was accomplished by saturating the source region with D2O vapor. The generated ions were guided through three differentially pumped stages using RF-only hexapole guides. The ions were collisionally cooled and stored in a 3D quadrupole Paul trap (Jordan TOF) attached to the second stage of a closed-cycle helium cryostat (Sumitomo). The trap was held at 28 K, enabling the formation of weakly bound N2 messenger tag complexes with the parent ions. The N2 was derived from trace impurities in the helium buffer gas. An RF sweeping field applied to the trap entrance electrode at the secular frequency of the untagged parent ion removed the parent ions from the trap. The remaining tagged ions were then excited by the output of a tunable optical parametric oscillator/amplifier (OPO/OPA) system (LaserVision) that was pumped by a Nd:YAG laser (Continuum Surelite EX, 1064 nm, 10 Hz, 7 ns, 660 mJ/ pulse). The output of the OPO/OPA is tunable between 2100 and 4500 cm⁻¹ with about 3 cm⁻¹ resolution. For excitation in the lower-frequency 1000-2100 cm⁻¹ range, the signal and idler outputs of the OPA were difference frequencies mixed in

AgGaSe₂. Following excitation, the ions were extracted into a reflectron time-of-flight mass spectrometer and detected with a dual MCP detector. The tag-loss photofragmentation yield was recorded as a function of laser frequency to measure the vibrational action spectrum. The spectra were normalized to the output laser power, which has a large variation over the tuning range. Spectra in the higher-frequency region were collected at reduced laser powers to ensure linearity. The presented spectra were averages of approximately 20 scans.

COMPUTATIONAL METHODS

The computational strategies employed here were described in more detail previously 29,30,32,33 and will be briefly summarized. The positions of all atoms except for the shared H atom were described using the Z-matrix coordinate representation. The shared H atom was described by the Cartesian coordinates $\{x, y, z\}$ based on a localized reference frame relative to the positions of the remaining atoms. The x-axis lies along the O-N donor—acceptor axis with the origin at the midpoint between these two atoms. The y-axis is perpendicular to the x-axis and lies in the plane defined by the N, O, and C atoms directly below the O atom (see Figure 1). The z-axis follows directly from these two definitions.

The Wilson F and G matrices³⁴ were then calculated at the equilibrium configuration, where the F matrix is calculated from the Hessian obtained in a Gaussian frequency calculation.³⁵ All calculations were carried out at the B3LYP/6-311+G(d,p) level of theory. The $\{x, y\}$ degrees of freedom were decoupled from the remaining internal degrees of freedom by zeroing the appropriate elements of the F and G matrices. The zeroed elements of the latter matrix were small based on the coordinate choice. Diagonalizing these two matrices leads to a set of normal coordinates that, when combined with the $\{x, y\}$ coordinates, fully describe the internal degrees of freedom.

The potential was expanded in terms of the normal coordinates to second order as

$$V = V_0 - \mathbf{f}^{\mathrm{T}} \mathbf{Q} + \frac{1}{2} \mathbf{Q}^{\mathrm{T}} \mathcal{F} \mathbf{Q}$$
 (1)

where $\{V_0, \mathbf{f}, \mathcal{F}\}$ are the potential, forces, and force constant matrix written as functions of x and y when all remaining coordinates are held at their equilibrium values. The dipole and its derivatives were calculated as

$$\mathbf{d} = \mathbf{d}_0 + \mathbf{D}^{\mathrm{T}} \mathbf{Q} \tag{2}$$

where $\{\mathbf{d}_0, \mathbf{D}\}$ are the dipole components and their derivatives calculated in an Eckart frame. The $\{x, y\}$ dependencies of the potential and dipole parameters were modeled on a grid of points that were used as input for a discrete variable representation (DVR) calculation.

The full Hamiltonian takes the form $\hat{H} = \hat{T} + \hat{V}$, where the potential is given by eq 1. The coordinate choice leads to a simple approximate form for the kinetic energy contribution

$$\hat{T} = \frac{1}{2} [G_{xx} p_x^2 + G_{yy} p_y^2] + \frac{1}{2} \sum_i P_i^2$$
(3)

where P_i is the normal coordinate momentum. The kinetic contribution was treated at the harmonic level, and the coordinate dependencies of the Wilson G-matrix elements were ignored. The kinetic coupling of the $\{x, y\}$ degrees of freedom to the other vibrational coordinates was also

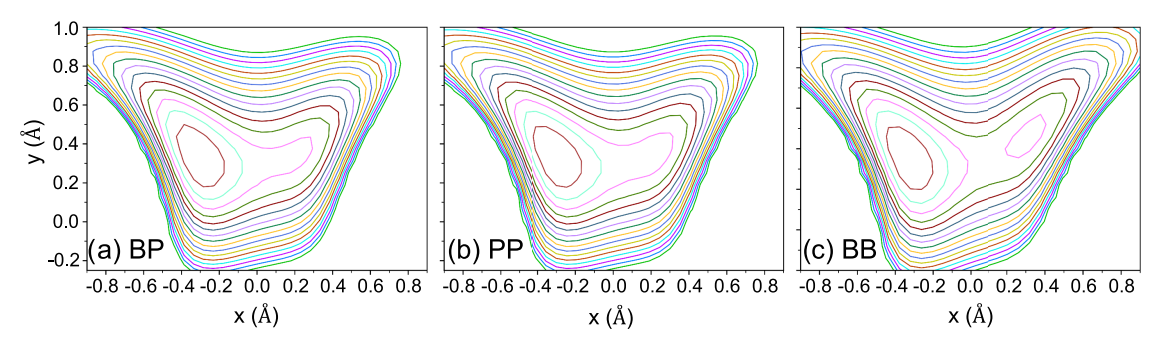


Figure 3. Equipotential energy curves for V_0 of eq 1 as a function of the $\{x, y\}$ coordinates of the phenol H atom for the three dyad species of Figure 1 with all other atoms fixed at their equilibrium positions. (a) BP, (b) PP, (c) BB. The contours are spaced at 1000 cm⁻¹ intervals and result from a two-dimensional cubic spline fit. The potentials clearly show the influence of the two possible binding sites for the H atom.

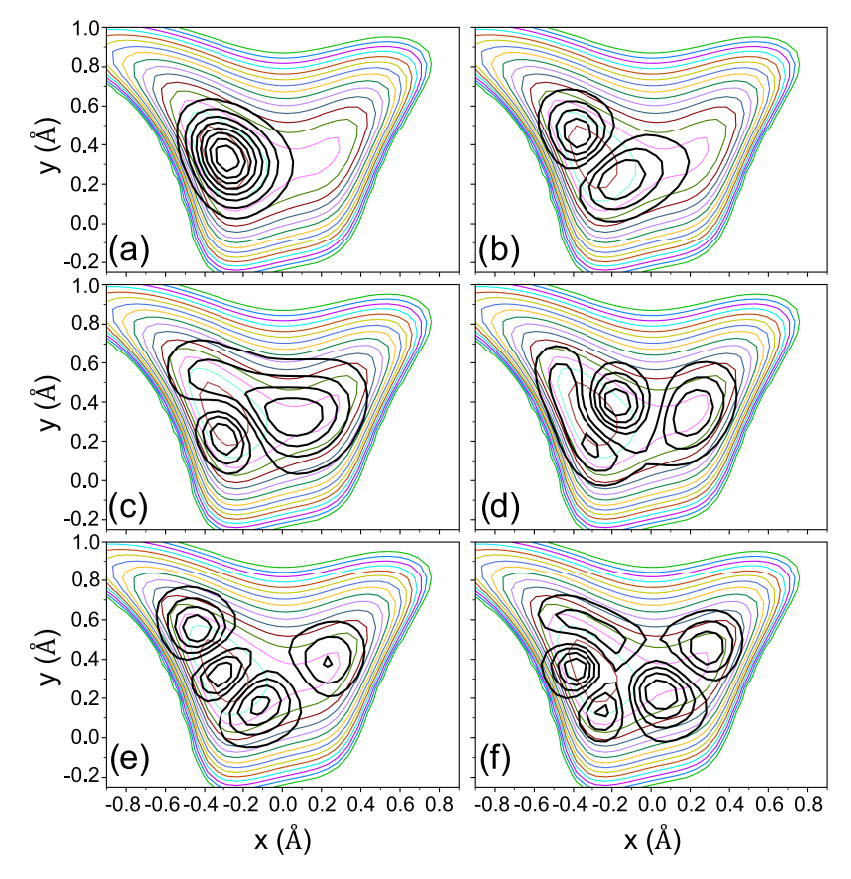


Figure 4. Six lowest-energy wavefunctions (black) corresponding to n = 1-6 of eq 5 describing the H atom $\{x, y\}$ degrees of freedom of dyad BP. (a) Ground state Ψ_1 . (b) Ψ_2 represents one quantum in the in-plane OH bend. (c) Ψ_3 nominally corresponds to one quantum in the OH stretch but shows clear bend character. (d) Ψ_4 and (e) Ψ_5 qualitatively resemble the stretch and bend overtones, respectively. (f) Ψ_6 is not easily described in a local mode harmonic picture. The wavefunctions indicate significant dislocation of the H atom along the transfer coordinate upon vibrational excitation.

neglected. This coupling is small due to the light proton and the choice of the $\{x, y\}$ internal coordinates. G_{xx} and G_{yy} were set to the equilibrium values of 1.0280 and 1.0266 amu⁻¹, respectively, for BP and PP. For BB, the equilibrium values for G_{xx} and G_{yy} were 1.0282 and 1.0268 amu⁻¹, respectively.

The contributions that depend solely on the $\{x, y\}$ degrees of freedom were used to define the H atom Hamiltonian

$$\hat{H}^{x,y} = \frac{1}{2} [G_{xx} p_x^2 + G_{yy} p_y^2] + V_0$$
(4)

The associated eigenfunctions and eigenvalues were solved using a sinc DVR³⁶ based on a 31 \times 24 grid of {x, y} points. Only those \sim 500 points for which V_0 was less than 19,000

cm⁻¹ were included in the 2D-DVR calculations. The eigenkets were expressed as linear combinations of the DVR kets $|\chi_k\rangle$ centered on the points $\{x_k, y_k\}$ as

$$|\Psi_n\rangle = \sum_k |\chi_k\rangle \langle \chi_k |\Psi_n\rangle \tag{5}$$

The eigenvalues are written as $E_n^{(x, y)}$. Based on previous studies, the number of grid points used is expected to yield eigenvalues that are accurate to 1 cm⁻¹ for the 10 lowest states.

The final Hamiltonian was set up as a direct product of N of the lowest-energy kets described above and a harmonic oscillator basis |v⟩ describing a subset K of the Q degrees of freedom. For a given subset K, the specific normal modes

chosen for inclusion in the basis were selected as follows. The value f_i^2/\mathcal{F}_{ii} was evaluated in wavenumbers at the midpoint for the H atom transfer. The K-1 normal modes with the largest value of this metric were included in addition to the normal mode that closely approximated the out-of-plane OH motion.

The sum of products form of the potential in eq 1 leads to easy evaluation of the matrix elements. Evaluating the full Hamiltonian matrix only requires linear and quadratic simple harmonic oscillator matrix elements of the position and momentum operators. The size of the harmonic oscillator basis $|\mathbf{v}\rangle$ was controlled by a single parameter M. Only those basis functions for which $\sum_i v_i$ is less than M, where v_i are the normal mode quantum numbers, were included in the basis.

The Hamiltonian in the $|\Psi_n\rangle|\mathbf{v}\rangle$ basis has many zero elements and is ideal for iterative methods for solving the Schrödinger equation. To obtain vibrational spectra, the three-stage approach of Stanton was followed. First, the Davidson method was used to calculate the ground-state eigenfunction, $|\Phi_{gs}\rangle$, of the full Hamiltonian as a linear combination of the basis $|\Psi_n\rangle|\mathbf{v}\rangle$. We next evaluated $d_x|\Phi_{gs}\rangle$ and $d_y|\Phi_{gs}\rangle$, where d_x and d_y are the in-plane components of the dipole given by eq 2. The d_x and d_y vectors were the starting vectors of the Lanczos method, which, as an output, provides the eigenvalues E_k and the eigenfunction expansion coefficients $A_{a,k} = \langle \Phi_k | d_a | \Phi_{gs} \rangle$. The spectral intensities were calculated as

$$I_k = (A_{x,k}^2 + A_{y,k}^2)E_k (6)$$

The z-components of the dipole were included in initial studies, but their contribution to the spectra under consideration was found to be negligible.

■ RESULTS AND DISCUSSION

H Atom Potentials and Dislocation. The two-dimensional potentials describing the H atom $\{x, y\}$ degrees of freedom are presented in Figure 3. The global minimum position of the H atom at the phenol O atom site occurs around {-0.3, 0.3 Å} in each dyad. Each potential also exhibits a soft shelf with a local minimum at the N atom site about 3000 cm⁻¹ higher in energy. BB has the deepest and most localized N atom minimum around {0.3, 0.5 Å}. In contrast, the N atom minima in BP and PP occur around {0.2, 0.3 Å} and are quite shallow and broad. Despite having the same phenol-pyridine motif, the subtle influences from the identity of the charged group appended at the para position can clearly be seen in the BP and PP potentials. The differences between the potentials are consistent with the structural variations among the dyads. BP and PP have shorter O-N equilibrium distances of 2.54 and 2.53 Å, respectively, compared to 2.56 Å in BB. The shorter O-N distances in BP and PP result, in part, from the larger bond angles in the six-membered pyridine ring compared to the five-membered imidazole ring. The shallow nature of the H atom potentials and close proximity of the O and N binding sites, therefore, are expected to have a significant impact on the OH vibrational modes.

The H atom wavefunctions for the six lowest-energy eigenstates of BP are shown superimposed on the 2D potential in Figure 4. Those for PP and BB are qualitatively similar and are presented in Supporting Information Figures S1 and S2, respectively. The lowest-energy state corresponds to the ground vibrational level (Figure 4a). The ground-state wavefunction Ψ_1 is largely localized to the O atom site, although modest probability amplitude extends toward the H

atom transfer midpoint. The Ψ_2 state shows probability amplitude along the COH in-plane bending coordinate (Figure 4b), and we qualitatively describe this state as one quantum in the OH bend. The Ψ_3 state (Figure 4c) shows amplitude along both the COH bending and OH-N stretching coordinates, indicating strong mixing of the bending and stretching H atom degrees of freedom. For simplicity, we qualitatively describe this state as one quantum in the OH stretch. Importantly, the Ψ_3 wavefunction predicts significant dislocation of the H atom along the transfer coordinate upon excitation of this state. The remaining three states are difficult to describe in a local mode harmonic picture. The Ψ_4 (Figure 4d) and Ψ_5 (Figure 4e) states most closely resemble the OH stretch and bend overtones, respectively. Given the substantial bend-stretch mixing and dislocation over both H atom sites, however, the description of these higher-energy states as overtones is qualitative at best. We emphasize that these calculations were performed in the ground electronic state with all other atoms held fixed at their equilibrium positions. The calculations, therefore, predict that the eigenfunctions of the H atom are strongly influenced by the N atom site even when all other modes are held frozen such that dislocation of the H atom between the donor and acceptor sites upon vibrational excitation is expected in these dyad systems even at 0 K.

The transition energies from the ground vibrational state to the five higher-energy eigenstates $(\Delta E_{n1}^{(x, y)} = E_n^{(x, y)} - E_1^{(x, y)})$ are given in Table 1 for the three dyads. The very soft and shallow

Table 1. Transition Energies ($\Delta E_{\rm NI}^{(x,\,y)}$, cm⁻¹) from the Ψ_1 Eigenstate to the Five Higher-Energy States Depicted in Figures 4 and 5 for the Light and Deuterated Isotopologues of the Three Dyads

		transition energy (cm^{-1})				
compound	isotopologue	$\Delta E_{21}^{\mathrm{xy}}$	$\Delta E_{31}^{\mathrm{xy}}$	$\Delta E_{41}^{ m xy}$	$\Delta E_{51}^{\mathrm{xy}}$	$\Delta E_{61}^{\mathrm{xy}}$
BP	h_3	1362	1951	2607	2805	3556
	d_3	1017	1654	2003	2273	2751
PP	h_2	1344	1870	2533	2776	3479
	d_2	1014	1608	1988	2165	2680
BB	h_4	1407	2078	2479	2785	3303
	d_4	1032	1759	2040	2362	2704

potentials result in the nominal OH stretch fundamental transitions, $\Delta E_{31}^{(x, y)}$, being highly red-shifted with transition frequencies between 1850 and 2100 cm⁻¹. These large red shifts are consistent with our previously reported results from vibrational second-order perturbation theory (VPT2) calculations, which placed the OH stretch fundamentals around 2200 cm⁻¹. Just as surprising are the frequencies of the qualitative stretch and bend overtone transitions, $\Delta E_{41}^{(x,y)}$ and $\Delta E_{51}^{(x, y)}$, respectively. The OH stretch overtones occur near 2500 cm⁻¹, only several hundred wavenumbers higher than the corresponding fundamentals. In contrast, the OH bend overtones for BP and PP occur at more than double the frequency of the fundamentals. We again emphasize that the description of these states as overtones is highly qualitative given the mixing of the H atom degrees of freedom. Comparisons, therefore, to typical slightly anharmonic oscillators are not straightforward. Nevertheless, the calculations highlight the unique influence of the very soft H atom potentials on the OH vibrational transitions in the dyad systems.

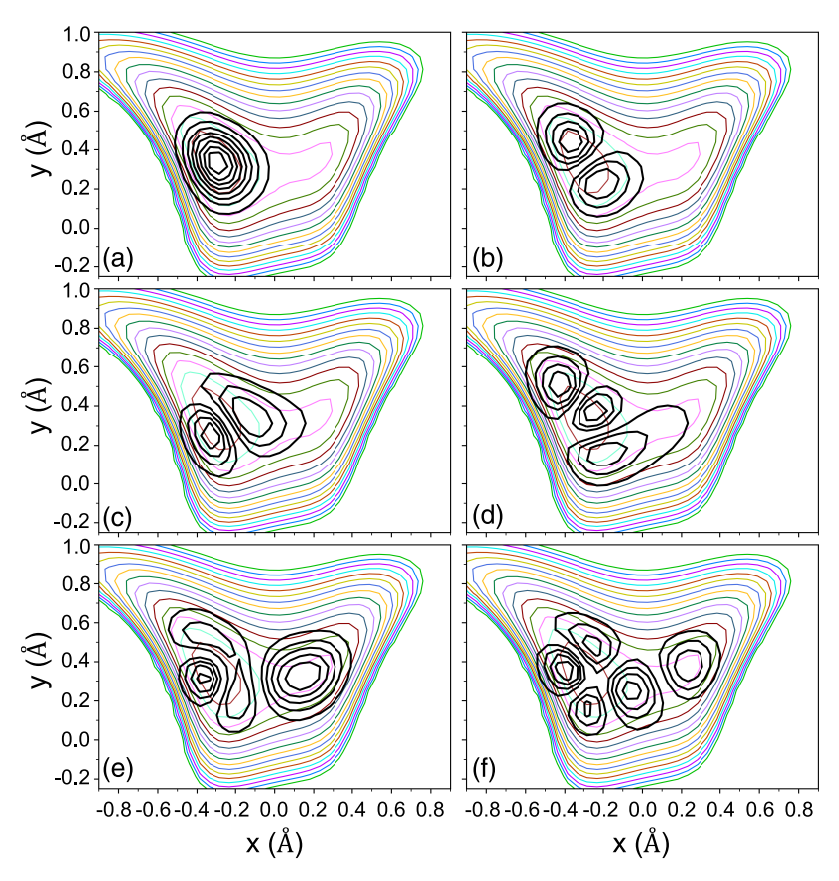


Figure 5. Six lowest-energy wavefunctions (black) corresponding to n = 1-6 of eq 5 describing the D atom $\{x, y\}$ degrees of freedom of deuterated dyad BP. (a) Ground state Ψ_1 . (b) Ψ_2 represents one quantum in the in-plane OD bend. (c) Ψ_3 corresponds to one quantum in the OD stretch. (d) Ψ_4 and (e) Ψ_5 qualitatively resemble the bend and stretch overtones, respectively. (f) Ψ_6 is not easily described in a local mode harmonic picture. The wavefunctions display less dislocation and bend-stretch mixing compared to the light isotopologue shown in Figure 4.

For comparison, the D atom wavefunctions for the deuterated d_3 isotopolgues of BP are presented in Figure 5. Those for PP and BB are given in Figures S3 and S4, respectively, and are again qualitatively similar. As expected, the wavefunction for the ground vibrational state Ψ_1 (Figure 5a) and OD bend fundamental ($\Psi_{\mathcal{D}}$ Figure 5b) are more localized to the O atom site compared to the light isotopologue. The Ψ_3 state (Figure 5b), representing the OD stretch fundamental, does exhibit appreciable dislocation of the D atom over the transfer coordinate. Compared to the light isotopologue, however, the D atom Ψ_3 state shows less apparent mixing between the bend and stretch degrees of freedom. The OD stretch fundamental frequencies, $\Delta E_{31}^{(x, y)}$, are still predicted to be abnormally red-shifted with transitions falling in the 1600-1750 cm⁻¹ range, about 0.85 times lower than the corresponding OH stretches for each dyad. In contrast to the light isotopologues, the qualitative OD bend overtones (Ψ_4 , Figure 5d) are now predicted to be lower in energy than the nominal OD stretch overtones (Ψ_5 , Figure 5e). The OD bend overtone transition frequencies, $\Delta E_{41}^{(x, y)}$, are predicted to occur around 2000 cm⁻¹, slightly less than double the bend fundamental frequencies. The OD stretch overtones, $\Delta E_{51}^{(x, y)}$, fall around 2200 cm⁻¹ and display large anharmonic shifts compared to the fundamental frequencies. The OD bends, therefore, appear to behave more like a typical anharmonic oscillator, while the OD stretches are still heavily influenced by the softness of the potentials along the transfer coordinate.

Vibrational Spectra. To investigate how the soft H atom potentials and dislocation manifest in the vibrational spectra, we employed the model Hamiltonian discussed above that couples the H atom $\{x, y\}$ degrees of freedom to the other normal mode coordinates. We include those normal coordinates that most strongly depend on the H atom $\{x, y\}$ potential. Since the H atom $\{x, y\}$ potential will depend strongly on the O-N distance, many of the normal coordinates included involve fluctuations in the O-N distance. The results for the three light isotopologues in the nominal OH stretch region are presented in Figure 6. Results for the full spectral range (1000-3600 cm⁻¹) are given in Figure S5. The notation $\{M, N, I, K\}$ indicates the values of the four parameters in the calculations that determine the size of the basis set. M is the size of the harmonic oscillator basis $|\mathbf{v}\rangle$ such that only those basis functions for which $\sum_i v_i < M$ are included. N is the number of H atom eigenstates, I is the number of Lanczos iterations, and K is the number of normal mode coordinates. Convergence was tested by varying the size of the basis sets, with examples given in Figure S6.

Interestingly, very little oscillator strength is predicted in the region of the expected OH stretch fundamentals near 1900 cm⁻¹. Similar to the predicted NH stretch region for excited-state methyl anthranilate, the intensity of the OH fundamentals appears to be distributed over many background states deriving from the harmonic basis that, consequently, results in the apparent absence of experimentally observed transitions. We note that the large number of normal modes needed (33) for convergence indicates the strong dependencies of the normal

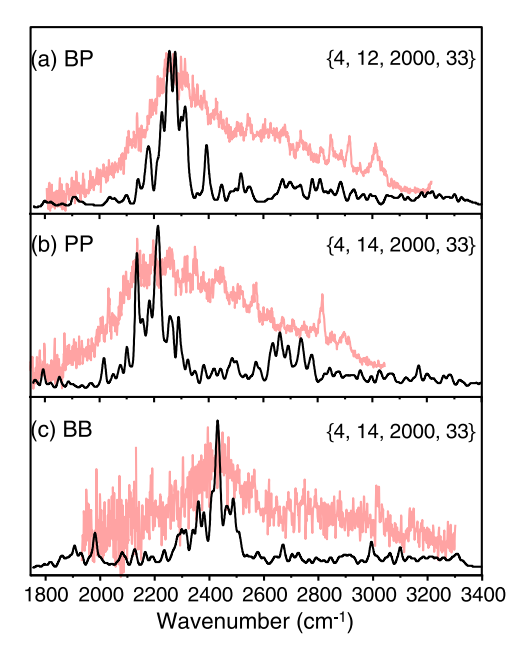


Figure 6. Calculated IR spectra of the light isotopologues in the OH stretch region using the model Hamiltonian described in the text. (a) BP, (b) PP, and (c) BB. The basis set is defined by the quantities $\{M, N, I, K\}$ discussed in the text. Individual transitions are modeled as Gaussian line shapes with FWHM = 7 cm⁻¹. The experimental spectra, shown in red, are red-shifted for better comparison to the calculated spectra.

mode degrees of freedom to H atom dislocation. It is likely that a larger basis set would yield further dilution of the transitions predicted in this spectral region.

The most intense transitions are predicted in the 2200–2600 cm $^{-1}$ region. It is difficult to discern from which H atom eigenstates the oscillator strength derives. Our time-dependent calculations (discussed below) indicate that the H atom eigenstates are themselves highly mixed. The oscillator strength, therefore, derives from a combination of the Ψ_3 , Ψ_4 , and Ψ_5 states. The complex nature of the H atom wavefunctions depicted in Figure 4 means that contributions ultimately arise from a superposition of OH bending and stretching motions.

Importantly, this region of more intense transitions reasonably accounts for the observed absorption onset features in the experimental spectra. While the predicted band centers are red-shifted compared to experiment (~100 cm⁻¹ for BB, ~200 cm⁻¹ for BP, ~300 cm⁻¹ for PP; experimental spectra in Figure 6 are shifted for better comparison), the spectral breadths and trends are consistent with the experimental spectra. For example, PP is predicted to have the most congested and broadest spectrum overall, while BB has the smallest breadth of transitions. Between 2500 and 3400 cm⁻¹, the calculations predict a near continuum of weak transitions in the region of the experimentally observed asymmetric shoulders. PP is predicted to have the strongest set of transitions in this region, while BB has the weakest, in line with the experimental spectra. Although not quantitative, the calculated spectra qualitatively reproduce the profile and overall breadth of the experimentally measured spectra.

The calculated spectra for the deuterated isotopologues are presented in Figure 7. The spectra are dominated by the fingerprint normal mode transitions that are included in the model Hamiltonian. A distribution of weak transitions is

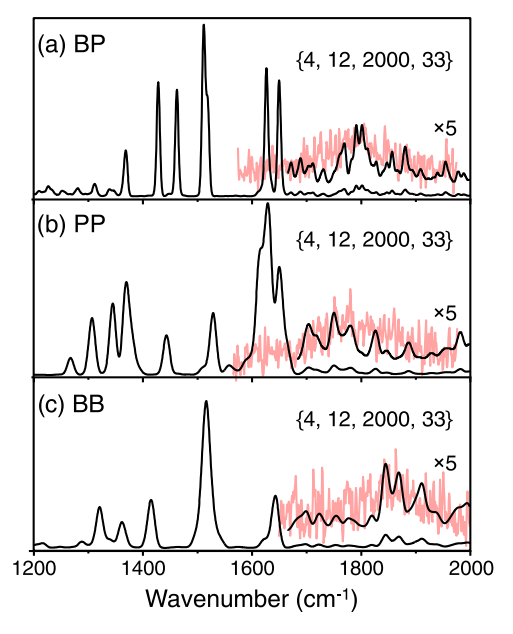


Figure 7. Calculated IR spectra of the deuterated isotopologues in the OD stretch region. (a) BP, (b) PP, and (c) BB. The basis set is defined by the quantities $\{M, N, I, K\}$ discussed in the text. Individual transitions are modeled as Gaussian line shapes with FWHM = $7 \, \mathrm{cm}^{-1}$. The weak bands of transitions deriving from the OD degrees of freedom are enlarged for clarity. The experimental spectra, shown in red, are red-shifted for better comparison to the calculated spectra.

predicted near 1800 cm⁻¹ that, like the calculated transitions for the light isotopologues, fall higher in energy than the expected OD stretch fundamentals. The computed spectra again qualitatively account for the weaker, more symmetrically broadened OD features experimentally measured in this region. Although the distribution of transitions is much narrower compared to the light isotopologues, the coupling of the OD eigenstates to the other normal modes remains significant within these dyad molecules. These observations are in stark contrast to those anticipated for deuterated methyl anthranilate, where a relatively sharp and largely uncoupled ND stretch transition was predicted in the electronic excited state. The strong coupling that remains in the deuterated dyads, therefore, results in a surprising degree of dilution of the OD oscillator strength over many background doorway states, leading to the relatively weak OD features in the experimental spectra.

Short-Time Dynamics. Short-time dynamics were investigated via numerical solutions of the time-dependent Schrödinger equation

$$\Psi(x, y, \mathbf{Q}, t) = \sum_{n} \sum_{\mathbf{v}} c_{n, \mathbf{v}}(t) |\Psi_{\mathbf{n}}\rangle |\mathbf{v}\rangle$$
(7)

using the method of Askar and Cakmak⁴⁰ in which the coefficients evolve as

$$\mathbf{c}(t + \Delta t) = \mathbf{c}(t - \Delta t) - 2i\Delta t \mathbf{H} \mathbf{c}(t)$$
(8)

This method complements the Lanczos method as both require matrix multiplication of the Hamiltonian matrix and a vector. Time steps of 0.033 fs were employed; 0.0167 fs steps yielded similar results.

The time-dependent approach allows us to connect with classical ideas of energy transfer. If a specific state of the $\{x, y\}$ degrees of freedom $|\Psi_n\rangle|\mathbf{v}\rangle$ were excited, time-dependent

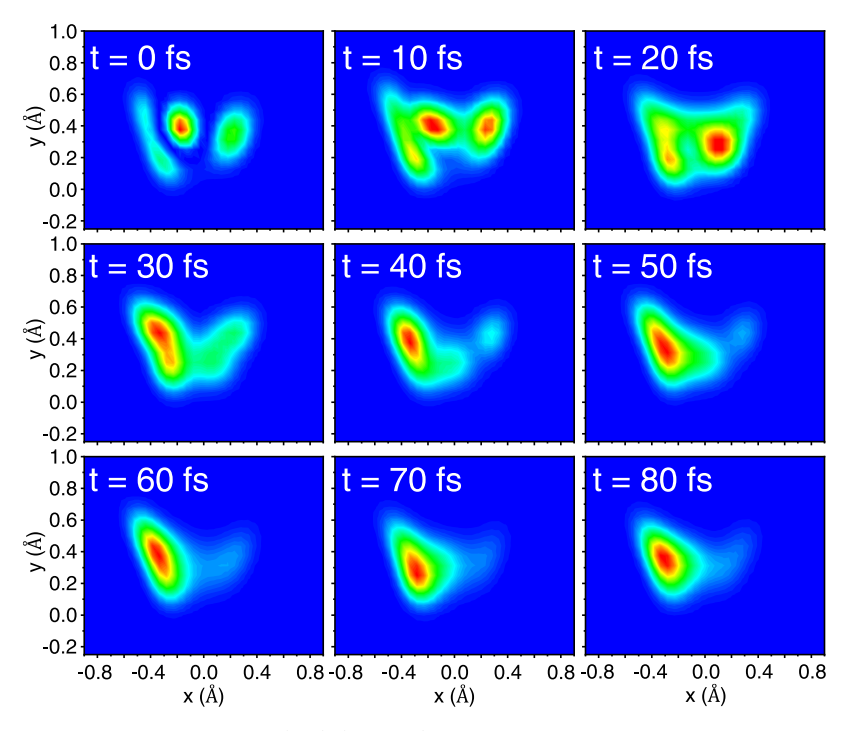


Figure 8. Evolution of the initially prepared probability P(x, y) (see eq 9) for excitation of state Ψ_4 of BP and no excitation in normal modes. The full wavefunction is averaged over the \mathbf{Q} degrees of freedom.

models can be used to follow the time evolution of this state and determine where energy flows in the molecule. Following Heller, ⁴¹ the Fourier transform of the overlap of a bright state with itself, $\langle \Psi_{\text{bright}} \ (t) | \Psi_{\text{bright}} \ (t=0) \rangle$, is proportional to the high-frequency portion of the spectrum.

Following ideas based on density matrices, integration over the Q degrees of freedom yields

$$P(x, y) = \int d\mathbf{Q} |\Psi(x, y, \mathbf{Q}, t)|^{2}$$

$$= \sum_{n} \sum_{m} \sum_{v} c_{m,v}^{*} c_{n,v} \Psi_{m}^{*}(x, y) \Psi_{n}(x, y)$$

$$\equiv \sum_{n} \sum_{m} d_{m,n} \Psi_{m}^{*}(x, y) \Psi_{n}(x, y)$$
(9)

where the diagonal elements $P_n = d_{n,n}$ are the probabilities of being in a given state $|\Psi_n\rangle$ of the $\{x,y\}$ degree of freedom of the system. Figure 8 shows the time evolution of P(x,y) for an initial state $|\Psi_4\rangle$ of dyad BP (Figure 4d) with no excitation in the normal modes. There is a significant probability of the H atom being on the N site within the first 20 fs, which is then followed by rapid relaxation back to the $|\Psi_1\rangle$ ground state within 100 fs. This evolution exhibits complex H atom motion, which must be due to the couplings between the $|\Psi_n\rangle$ states. In other words, the $|\Psi_n\rangle$ states are expected to be highly mixed in a time-independent model. Similar behavior is seen for the time evolution of the $|\Psi_3\rangle$ state (Figure S7).

The time evolution of the normal mode energies from the initially prepared $|\Psi_4\rangle$ state is shown in Figure S8. Consistent with the rapid relaxation of the $|\Psi_4\rangle$ state shown in Figure 8, many normal modes transitions show instantaneous responses to the excitation of the H atom. The immediate relaxation of energy from the H atom modes into many of the normal mode coordinates corroborates the significant coupling predicted by the time-independent approach.

CONCLUSIONS

The vibrational spectra of PCET dyad molecules in the nominal OH and OD stretch regions are calculated using a model Hamiltonian that couples the two-dimensional in-plane H atom degrees of freedom to the other normal mode coordinates. The strong intramolecular H-bonding interactions between the phenol H atom donor and N-heterocyclic base acceptor result in soft potentials that exhibit low-energy pathways to H atom transfer. The calculated H atom vibrational wavefunctions show significant mixing between the bending and stretching coordinates and large probability amplitudes across the transfer coordinate. Vibrational excitation of these modes, therefore, is expected to yield substantial dislocation of the H atom between the donor and acceptor sites in the ground electronic state.

The extremely soft H atom potentials cause large forces to be exerted on the other normal mode coordinates during dislocation. Consequently, strong coupling is predicted between the H atom degrees of freedom and over two dozen normal modes. Many of these normal modes exhibit fluctuations in the key O-N donor-acceptor coordinate. The calculated vibrational spectra indicate that the oscillator strength of the highly red-shifted OH fundamental transition is diluted over many background states deriving from the normal mode basis. The strongest transitions are predicted to occur in the region of the nominal OH bend and stretch overtones. The calculated spectra qualitatively reproduce the experimentally measured absorption onset bands and broad asymmetric shoulders for each dyad. The computational model also predicts relatively strong coupling in the deuterated isotopologues, and the calculated spectra qualitatively reproduce the weak and symmetrically broadened experimentally measured OD features.

Finally, time-dependent calculations indicate initial rapid H atom dislocation to the N atom site followed by relaxation to

the ground vibrational state within 100 fs. Instantaneous responses from the coupled normal modes occur upon excitation of the H atom eigenstates. The rapid energy flow out of the initially excited H atom eigenstates corroborates the strong coupling predicted between not only the H atom and normal modes but also between the H atom eigenstates. The time-dependent calculations do not include explicit variations in the O–N distance. Given the strong coupling between the H atom and a multitude of low-frequency soft modes that yield O–N displacement, and rapid relaxation pathways, we anticipate that vibrational enhancement effects will play an important role in PCET dynamics within this class of model systems.

Critically, the calculations provide new physical insight into the origins of the uniquely broadened OH and OD vibrational features recorded in an important class of PCET model systems. The incredibly soft H atom potentials along the transfer coordinate result in OH vibrational states with strongly mixed bend-stretch character that cannot be easily described. Crucially, typical anharmonic oscillator effects and computational treatments are not sufficient to explain the experimental spectra. Our results show the importance of accurately coupling highly anharmonic reactive H atom/ proton transfer potential energy surfaces with other internal vibrational degrees of freedom to reveal the vibrational spectral signatures that manifest from strongly shared, dislocated, and transferring H atoms/protons in reactive systems. Given that the Tyr_Z-His₁₉₀ pair and other biologically important Hbonded systems have similarly short (~2.5 Å) donor-acceptor distances, these results provide an improved connection between the shape of a proton transfer potential energy surface and the vibrational spectrum, and lay the foundations for direct infrared spectroscopic studies of proton transfer processes.

ASSOCIATED CONTENT

Supporting Information

The Supporting Information is available free of charge at https://pubs.acs.org/doi/10.1021/acs.jpca.3c00524.

H atom wavefunctions for dyad PP (Figure S1); H atom wavefunctions for dyad BB (Figure S2); D atom wavefunctions for PP (Figure S3); D atom wavefunctions for BB (Figure S4); calculated spectra for the full $1000-3600~{\rm cm}^{-1}$ spectral range (Figure S5); calculated spectra of BP with different parameter values $\{M, N, I, K\}$ (Figure S6); time evolution of normal mode energies in BP after initial excitation of the $|\Psi_4\rangle$ state (Figure S7); time evolution of the initially prepared probability P(x, y) for excitation of state $|\Psi_3\rangle$ of BP (PDF)

AUTHOR INFORMATION

Corresponding Authors

Edwin L. Sibert III — Department of Chemistry and Theoretical Chemistry Institute, University of Wisconsin-Madison, Madison, Wisconsin 53706, United States; orcid.org/0000-0003-2752-1044; Email: elsibert@wisc.edu

Joseph A. Fournier — Department of Chemistry, Washington University in St. Louis, St. Louis, Missouri 63130, United States; orcid.org/0000-0001-7569-9176; Email: jfournier@wustl.edu

ī

Author

Liangyi Chen – Department of Chemistry, Washington University in St. Louis, St. Louis, Missouri 63130, United States; Occid.org/0000-0002-9391-4332

Complete contact information is available at: https://pubs.acs.org/10.1021/acs.jpca.3c00524

Notes

The authors declare no competing financial interest.

ACKNOWLEDGMENTS

E.L.S. gratefully acknowledges support from the National Science Foundation (NSF) via Grant CHE-1900095. J.A.F. acknowledges support from NSF through a CAREER Award (Grant CHE-2044927).

REFERENCES

- (1) Weinberg, D. R.; Gagliardi, C. J.; Hull, J. F.; Murphy, C. F.; Kent, C. A.; Westlake, B. C.; Paul, A.; Ess, D. H.; McCafferty, D. G.; Meyer, T. J. Proton-Coupled Electron Transfer. *Chem. Rev.* **2012**, *112*, 4016–4093.
- (2) Darcy, J. W.; Koronkiewicz, B.; Parada, G. A.; Mayer, J. M. A Continuum of Proton-Coupled Electron Transfer Reactivity. *Acc. Chem. Res.* **2018**, *51*, 2391–2399.
- (3) Migliore, A.; Polizzi, N. F.; Therien, M. J.; Beratan, D. N. Biochemistry and Theory of Proton-Coupled Electron Transfer. *Chem. Rev.* **2014**, *114*, 3381–3465.
- (4) Reece, S. Y.; Nocera, D. G. Proton-Coupled Electron Transfer in Biology: Results from Synergistic Studies in Natural and Model Systems. *Annu. Rev. Biochem.* **2009**, *78*, 673–699.
- (5) Irebo, T.; Reece, S. Y.; Sjödin, M.; Nocera, D. G.; Hammarström, L. Proton-Coupled Electron Transfer of Tyrosine Oxidation: Buffer Dependence and Parallel Mechanisms. *J. Am. Chem. Soc.* **2007**, *129*, 15462–15464.
- (6) Markle, T. F.; Rhile, I. J.; DiPasquale, A. G.; Mayer, J. M. Probing Concerted Proton—Electron Transfer in Phenol—Imidazoles. *Proc. Natl. Acad. Sci. U.S.A.* **2008**, *105*, 8185—8190.
- (7) Huynh, M. T.; Mora, S. J.; Villalba, M.; Tejeda-Ferrari, M. E.; Liddell, P. A.; Cherry, B. R.; Teillout, A.-L.; Machan, C. W.; Kubiak, C. P.; Gust, D.; et al. Concerted One-Electron Two-Proton Transfer Processes in Models Inspired by the Tyr-His Couple of Photosystem II. ACS Cent. Sci. 2017, 3, 372–380.
- (8) Gagliardi, C. J.; Wang, L.; Dongare, P.; Brennaman, M. K.; Papanikolas, J. M.; Meyer, T. J.; Thompson, D. W. Direct Observation of Light-Driven, Concerted Electron—Proton Transfer. *Proc. Natl. Acad. Sci. U.S.A.* **2016**, *113*, 11106—11109.
- (9) Pagba, C. V.; McCaslin, T. G.; Chi, S.-H.; Perry, J. W.; Barry, B. A. Proton-Coupled Electron Transfer and a Tyrosine—Histidine Pair in a Photosystem II-Inspired β -Hairpin Maquette: Kinetics on the Picosecond Time Scale. *J. Phys. Chem. B* **2016**, *120*, 1259–1272.
- (10) Pannwitz, A.; Wenger, O. S. Photoinduced Electron Transfer Coupled to Donor Deprotonation and Acceptor Protonation in a Molecular Triad Mimicking Photosystem II. *J. Am. Chem. Soc.* **2017**, 139, 13308–13311.
- (11) Lymar, S. V.; Ertem, M. Z.; Lewandowska-Andralojc, A.; Polyansky, D. E. Role of Hydrogen Bonding in Photoinduced Electron—Proton Transfer from Phenols to a Polypyridine Ru Complex with a Proton-Accepting Ligand. *J. Phys. Chem. Lett.* **2017**, *8*, 4043—4048.
- (12) Zhang, M.-T.; Irebo, T.; Johansson, O.; Hammarström, L. Proton-Coupled Electron Transfer from Tyrosine: A Strong Rate Dependence on Intramolecular Proton Transfer Distance. *J. Am. Chem. Soc.* **2011**, *133*, 13224–13227.
- (13) Markle, T. F.; Zhang, M.-T.; Santoni, M.-P.; Johannissen, L. O.; Hammarström, L. Proton-Coupled Electron Transfer in a Series of Ruthenium-Linked Tyrosines with Internal Bases: Evaluation of a

- Tunneling Model for Experimental Temperature-Dependent Kinetics. *J. Phys. Chem. B* **2016**, *120*, 9308–9321.
- (14) Glover, S. D.; Parada, G. A.; Markle, T. F.; Ott, S.; Hammarström, L. Isolating the Effects of the Proton Tunneling Distance on Proton-Coupled Electron Transfer in a Series of Homologous Tyrosine-Base Model Compounds. J. Am. Chem. Soc. 2017, 139, 2090–2101.
- (15) Johannissen, L. O.; Irebo, T.; Sjodin, M.; Johansson, O.; Hammarstrom, L. The Kinetic Effect of Internal Hydrogen Bonds on Proton-Coupled Electron Transfer from Phenols: A Theoretical Analysis with Modeling of Experimental Data. *J. Phys. Chem. B* **2009**, 113, 16214–16225.
- (16) Hay, S.; Scrutton, N. S. Good Vibrations in Enzyme-Catalysed Reactions. *Nat. Chem.* **2012**, *4*, 161–168.
- (17) Layfield, J. P.; Hammes-Schiffer, S. Hydrogen Tunneling in Enzymes and Biomimetic Models. *Chem. Rev.* **2014**, *114*, 3466–3494.
- (18) Manbeck, G. F.; Fujita, E.; Concepcion, J. J. Proton-Coupled Electron Transfer in a Strongly Coupled Photosystem II-Inspired Chromophore–Imidazole–Phenol Complex: Stepwise Oxidation and Concerted Reduction. *J. Am. Chem. Soc.* **2016**, *138*, 11536–11549.
- (19) Yoneda, Y.; Mora, S. J.; Shee, J.; Wadsworth, B. L.; Arsenault, E. A.; Hait, D.; Kodis, G.; Gust, D.; Moore, G. F.; Moore, A. L. Electron–Nuclear Dynamics Accompanying Proton-Coupled Electron Transfer. J. Am. Chem. Soc. 2021, 143, 3104–3112.
- (20) Chen, L.; Fournier, J. A. Probing Hydrogen-Bonding Interactions within Phenol-Benzimidazole Proton-Coupled Electron Transfer Model Complexes with Cryogenic Ion Vibrational Spectroscopy. J. Phys. Chem. A 2021, 125, 9288–9297.
- (21) Chen, L.; Ma, Z.; Fournier, J. A. Origins of the Diffuse Shared Proton Vibrational Signatures in Proton-Coupled Electron Transfer Model Dyad Complexes. *J. Chem. Phys.* **2022**, *157*, No. 154308.
- (22) DeBlase, A. F.; Bloom, S.; Lectka, T.; Jordan, K. D.; McCoy, A. B.; Johnson, M. A. Origin of the Diffuse Vibrational Signature of a Cyclic Intramolecular Proton Bond: Anharmonic Analysis of Protonated 1, 8-Disubstituted Naphthalene Ions. *J. Chem. Phys.* 2013, 139, No. 24301.
- (23) Leavitt, C. M.; DeBlase, A. F.; Johnson, C. J.; van Stipdonk, M.; McCoy, A. B.; Johnson, M. A. Hiding in Plain Sight: Unmasking the Diffuse Spectral Signatures of the Protonated N-Terminus in Isolated Dipeptides Cooled in a Cryogenic Ion Trap. *J. Phys. Chem. Lett.* **2013**, *4*, 3450–3457.
- (24) Wolke, C. T.; DeBlase, A. F.; Leavitt, C. M.; McCoy, A. B.; Johnson, M. A. Diffuse Vibrational Signature of a Single Proton Embedded in the Oxalate Scaffold, HO₂CCO₂. *J. Phys. Chem. A* **2015**, *119*, 13018–13024.
- (25) Robertson, W. H.; Price, E. A.; Weber, J. M.; Shin, J.-W.; Weddle, G. H.; Johnson, M. A. Infrared Signatures of a Water Molecule Attached to Triatomic Domains of Molecular Anions: Evolution of the H-Bonding Configuration with Domain Length. *J. Phys. Chem. A* **2003**, *107*, 6527–6532.
- (26) Myshakin, E. M.; Jordan, K. D.; Sibert, E. L., III; Johnson, M. A. Large Anharmonic Effects in the Infrared Spectra of the Symmetrical CH₃NO₂⁻•(H₂O) and CH₃CO₂⁻•(H₂O) Complexes. *J. Chem. Phys.* **2003**, *119*, 10138−10145.
- (27) Heine, N.; Kratz, E. G.; Bergmann, R.; Schofield, D. P.; Asmis, K. R.; Jordan, K. D.; McCoy, A. B. Vibrational Spectroscopy of the Water—Nitrate Complex in the O–H Stretching Region. *J. Phys. Chem. A* **2014**, *118*, 8188–8197.
- (28) Craig, S. M.; Menges, F. S.; Duong, C. H.; Denton, J. K.; Madison, L. R.; McCoy, A. B.; Johnson, M. A. Hidden Role of Intermolecular Proton Transfer in the Anomalously Diffuse Vibrational Spectrum of a Trapped Hydronium Ion. *Proc. Natl. Acad. Sci. U.S.A.* 2017, 114, E4706–E4713.
- (29) Blodgett, K. N.; Fischer, J. L.; Zwier, T. S.; Sibert, E. L. The Missing NH Stretch Fundamental in S₁ Methyl Anthranilate: IR-UV Double Resonance Experiments and Local Mode Theory. *Phys. Chem. Chem. Phys.* **2020**, 22, 14077–14087.
- (30) Sibert, E. L.; Blodgett, K. N.; Zwier, T. S. Spectroscopic Manifestations of Indirect Vibrational State Mixing: Novel Anhar-

- monic Effects on a Prereactive H Atom Transfer Surface. J. Phys. Chem. A 2021, 125, 7318-7330.
- (31) Chen, L.; Dean, J. L. S.; Fournier, J. A. Time-Domain Vibrational Action Spectroscopy of Cryogenically Cooled, Messenger-Tagged Ions Using Ultrafast IR Pulses. *J. Phys. Chem. A* **2021**, *125*, 10235–10244.
- (32) Carrington, T., Jr; Miller, W. H. Reaction Surface Description of Intramolecular Hydrogen Atom Transfer in Malonaldehyde. *J. Chem. Phys.* **1986**, *84*, 4364–4370.
- (33) Barnes, G. L.; Sibert, E. L., III The Effects of Asymmetric Motions on the Tunneling Splittings in Formic Acid Dimer. *J. Chem. Phys.* **2008**, *129*, No. 164317.
- (34) Wilson, E. B.; Decius, J. C.; Cross, P. C. Molecular Vibrations: the Theory of Infrared and Raman Vibrational Spectra; McGraw-Hill: New York, 1955; p 388.
- (35) Frisch, M. J.; Trucks, G. W.; Schlegel, H. B.; Scuseria, G. E.; Robb, M. A.; Cheeseman, J. R.; Scalmani, G.; Barone, V.; Petersson, G. A.; Nakatsuji, H. *Gaussian 16*; Gaussian, Inc.: Wallingford, CT, 2016.
- (36) Colbert, D. T.; Miller, W. H. A Novel Discrete Variable Representation for Quantum Mechanical Reactive Scattering via the S-matrix Kohn Method. *J. Chem. Phys.* **1992**, *96*, 1982–1991.
- (37) Stanton, J. F. On the Vibronic Level Structure in the NO₃ Radical: II. Adiabatic Calculation of the Infrared Spectrum. *Mol. Phys.* **2009**, *107*, 1059–1075.
- (38) Davidson, E. R. Methods in Computational Molecular Physics; Diercksen, G. H. F.; Wilson, S., Eds.; NATO Advanced Study Institute, Series C. Plenum: New York, 1983; Vol. 113.
- (39) Cullum, J. K.; Willoughby, R. A. Lanczos Algorithms for Large Symmetric Eigenvalue Computations: Vol. 1: Theory; SIAM: Boston, 1985; Vol. 41.
- (40) Askar, A.; Cakmak, A. S. Explicit Integration Method for the Time-dependent Schrodinger Equation for Collision Problems. *J. Chem. Phys.* **1978**, *68*, 2794–2798.
- (41) Heller, E. J.; Stechel, E. B.; Davis, M. J. Molecular Spectra, Fermi Resonances, and Classical Motion. *J. Chem. Phys.* **1980**, 73, 4720–4735.